ELSEVIER

Contents lists available at ScienceDirect

Journal of Power Sources

journal homepage: www.elsevier.com/locate/jpowsour





Ti-Nb alloy coatings for anode PTLs in PEM water electrolyzers

Tim Sievert b, s, Sarah Zerressen b, Andreas Glüsen b, Martin Bram b, b, Sven Uhlenbruck b, Klaus Bender c, Frank Vondahlen b, Ping Xiao b, Xuezhen Cao b, Olivier Guillon b, Ralf Peters a, b, Martin Müller b, Ulf-Peter Apfel d, Robert Vaßen b, f

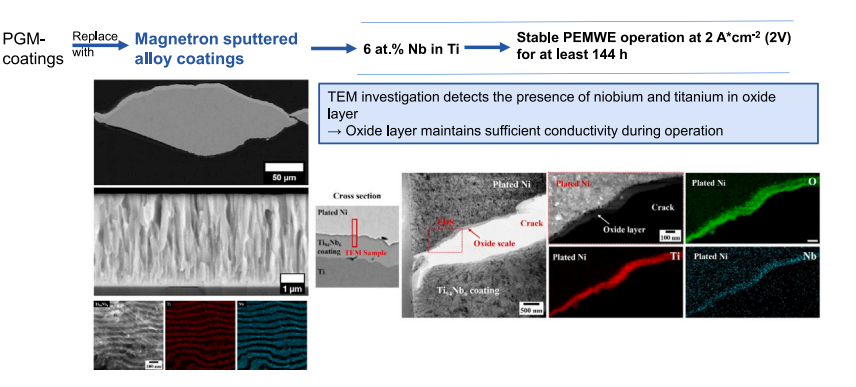
- ^a Forschungszentrum Jülich GmbH, Institute of Energy Technologies, IET-4: Electrochemical Process Engineering, 52425, Jülich, Germany
- b Forschungszentrum Jülich GmbH, Institute of Energy Materials and Devices, IMD-2: Materials Synthesis and Processing, 52425, Jülich, Germany
- c Bender GmbH Maschinenbau u. Streckmetallfabrik, 57078, Siegen, Germany
- ^d Ruhr-Universität Bochum, Inorganic Chemistry, 44801, Bochum, Germany
- e Fraunhofer UMSICHT, Department of Electrosynthesis, 46047, Oberhausen, Germany
- f Ruhr-Universität Bochum, Institute for Materials, 44801, Bochum, Germany
- g Jülich Aachen Research Alliance: JARA-Energy, 52425, Jülich, Germany
- h Department of Materials and Henry Royce Institute, University of Manchester, M13 9PL, Manchester, United Kingdom
- ⁱ Ruhr-Universität Bochum, Institute of Thermo- and Fluiddynamics, Synthetic Fuels, 44801, Bochum, Germany

HIGHLIGHTS

- Noble metal free Ti-Nb alloy coatings for anode PTLs in PEMWE.
- Sputtered alloy coatings enable stable PEMWE operation for at least 144 h.
- TEM investigation detects the presence of niobium and titanium in oxide layer.
- Mixed oxide layer maintains sufficient conductivity.

GRAPHICAL ABSTRACT

Ti-Nb alloy coatings for anode PTLs in PEM water electrolyzers



ARTICLE INFO

Keywords: Green hydrogen PTL coating PEMWE Titanium Niobium

ABSTRACT

One of the most cost-intensive components of proton exchange membrane water electrolyzers (PEMWE) are the anode-side Porous Transport Layers (PTLs), often comprised of titanium with a noble metal coating such as platinum. Replacing the noble metal coating is crucial to reduce the manufacturing costs of PEM electrolyzers. This study aims to replace conventional platinum coatings with titanium-niobium alloy coatings using magnetron sputtering. To evaluate the performance and stability of the coated PTLs, laboratory-scale tests have been conducted with PEMWE single cells. Post-mortem analysis of the PTLs included scanning electron microscopy (SEM), energy-dispersive X-ray spectroscopy (EDS), transmission electron microscopy (TEM) and resistance measurements. So far, the best results were achieved with alloy coatings consisting of 94 at.% titanium and 6 at.% niobium, as these coatings enabled stable PEMWE operation for 144 h at 2.0 V. TEM

E-mail address: t.sievert@fz-juelich.de (T. Sievert).

^{*} Corresponding author.

¹ These authors contributed equally to this work.

confirms that niobium is incorporated into the growing oxide scale. We assume that the pentavalent niobium atoms serve as donator sites in the oxide increasing its electric conductivity.

1. Introduction

Due to the highly oxidative conditions at the anode side in PEM water electrolysis cells, the catalyst-facing side of uncoated titanium PTLs form ${\rm TiO_2}$ scales resulting in an increased contact resistance and overvoltage. To prevent the formation of titanium oxide, PTLs are usually coated with precious metals such as platinum or iridium. These precious metals exhibit excellent electrochemical stability under the operating conditions. The stability and degradation of PTL coatings are primarily influenced by two factors: polarization by the electrochemical potential needed for the water splitting reaction to occur and contact with the highly acidic sulfonic acid groups of the polymer electrolyte (pK_a = -6 [1]). Although the stability of precious metals is unsurpassed [2], research into the reduction or replacement of precious metal coatings is important to lower the investment costs for PEM electrolysers [3–5].

To date, only two reports exist about noble-metal free PTL coatings for anode PTLs consisting of niobium. Stiber et al. [6] presented electrolysis operation for 1500 h with a niobium and sub-layer titanium coated stainless steel expanded mesh yielding an approximate ageing rate of $267\,\mu\text{V}\,h^{-1}$. Stein et al. [2] reported an ageing rate of $162\,\mu\text{V}\,h^{-1}$ with a Nb-coated PTL in the second half of a 2000 h experiment. These ageing rates might be caused by the fact that the thermodynamic equilibrium of niobium lies on the oxide side [7] at potentials of up to $1.5\,\text{V}$ to $1.8\,\text{V}$ vs. RHE (Reversible Hydrogen Electrode), which are to be expected at the anode catalyst [8–11]. Therefore, an increase in the resistance of the coating is expected during prolonged operation [12].

In addition to the search for pure metallic materials that are resistant to corrosion and oxidation, another viable approach could be to maintain the conductivity of the PTL surface by modifying the titanium surface in such a way that the oxide growth rate is decreased and the conductivity of the forming oxide layer remains sufficiently high. For example, Ramos et al. [13] reported a significant increase in the electrical conductivity of rutile TiO₂ upon niobium implantation. Furthermore, Pérez et al. [14] found that the growth of an oxide scale on titanium at 800°C in dry and humidified argon atmosphere with 20 % oxygen is significantly decreased when titanium is alloyed with 4 at.% Nb compared to pure titanium. Aukland et al. [15] investigated conductive Nb-Ti-alloys for fuel cell bipolar plate coatings with 1 at.%, 1.5 at.% and 3 at.% Nb where the latter exhibited the lowest resistance. Alloying elements like Ta and Nb are reported to reduce the solubility of oxygen in titanium [16] and to reduce the oxide thickness [14]. Gesesse et al. also report that doping TiO2 films with niobium significantly reduces the resistivity of the thin films [17] and Frisch et al. [18] calculated that for doping TiO₂, niobium is the element with the highest potential to enhance the electrical conductivity of the oxide.

However, studies about Ti–Nb alloy coatings on anode PTLs have, to the best of the authors' knowledge, not yet been published. Therefore, we investigated short- and midterm performance developments during 144 h or 672.5 h electrolysis operation at 2.0 V with magnetron sputtered Ti–Nb alloy coatings with 3 at.%, 6 at.% and 28 at.% Nb on two different types of titanium PTLs. These ratios were selected as Aukland et al. [15] found the lowest surface resistance for coatings containing 3 at.% Nb on bipolar plates and Frisch et al. [18] reported a maximum conductivity of Nb doped mesoporous titanium oxide with a Nb mole fraction of 33 at.%.

Table 1Deposition parameter of Ti-Nb alloys via magnetron sputtering.

	$Ti_{97}Nb_3$	Ti ₉₄ Nb ₆	${ m Ti}_{72}{ m Nb}_{28}$
Initial pressure /mbar	$4 \cdot 10^{-5}$	$4 \cdot 10^{-5}$	$4 \cdot 10^{-5}$
Process pressure /mbar	580	580	580
Ar-flow/sccm	280	280	280
Kr-flow/sccm	200	200	200
Cathode power 3x Ti-Target /W	5000	5000	4000
Cathode power 1x Nb-Target /W	500	1000	5000
Bias /V	-200	-200	-200
Sputter duration /s	4000	4000	4000

2. Materials and methods

2.1. Magnetron sputtering

All PTLs were cleaned before they were coated using an oil removing program operating at 95 °C in a laboratory dishwasher (Miele Professional PG 8583). Afterwards, the samples were dried using compressed air. The titanium expanded metals and felts were coated using a CC800/9 sputtering system from CemeCon AG. The samples were placed in the centre of the chamber on a rotating columnar sample holder. Three titanium and one niobium targets were arranged on the four sides of the rectangular chamber. First, the system was evacuated to an initial pressure of $4 \cdot 10^{-5}$ mbar and then heated to approximately 550 °C at the sample holder. Following an initial sputter etching step, the deposition process was initiated. The coating parameters for the three different coatings are summarized in Table 1. The coating composition was controlled by adjusting the power applied to the individual sputter targets. A higher target power results in a higher deposition rate and thus a higher contribution of the respective element to the coating. The coatings were deposited on (100) silicon wafers, titanium expanded metals (TiEM) and titanium felts (TiF).

2.2. Electron microscopy

To analyse the morphology and thickness of the alloy coatings, metallographic cross-sections were prepared and examined via SEM using a Zeiss EVO 15 instrument equipped with an Oxford Instruments Ultim Max 100 EDS detector. Coating thicknesses were measured using the software ImageJ. In addition, a TEM lamella from a sample was prepared by using a focused ion beam (FIB, Helios Nanolab 660) after electrolysis to investigate the oxide layer on the MEA-facing side. For this purpose, the sample was first galvanically coated with nickel before the lamella was cut and EDS analysis was performed. The TEM characterization and local chemical analysis were carried out on Talos 2 F200X equipped with EDS detector.

2.3. PEMWE test cells

In order to assess the newly produced PTLs under PEMWE conditions, the samples were installed in in-house-build laboratory-scale test cells (see Fig. 1c). A cell comprises two meander flow fields (FF, see Figure S1 in the supplementary information): one located on the anode side and the other on the cathode side providing water for the active cell area of $17.64\,\text{cm}^2$. The membrane electrode assemblies (MEAs) were produced inhouse by means of the decal method with Nafion 117 membrane ($\approx 180\,\mu\text{m}$ in dry state, The Chemours Company FC, LLC). The preparation of the catalyst layers (CLs) and MEAs has already been described in a previous study [19]. The catalyst loadings amounted for $0.99\pm0.15\,\text{mg}_{\text{Ir}}\text{cm}^{-2}$ (anode side) and $0.23\pm0.05\,\text{mg}_{\text{Pt}}\text{cm}^{-2}$ on the cathode side. Commercially available carbon PTLs (TGP-H-120 from

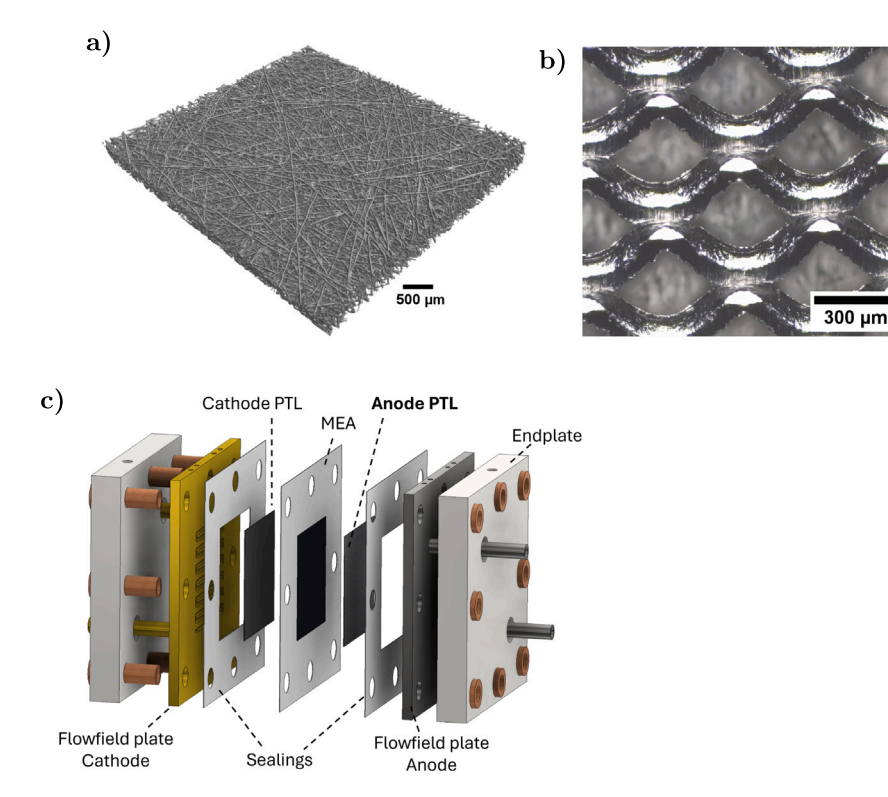


Fig. 1. (a) 3D X-ray tomograms of titanium felt from Bekaert, details about measurement parameters of computer tomography are given in the supplementary information, (b) Light microscopy image of titanium expanded mesh from Bender (TiEM) and (c) Illustration of the laboratory sized PEMWE test cell.

TORAY INDUSTRIES, INC.) with a thickness of 370 \pm 6 μm and porosity of 78 % served as PTLs on the cathode side. This carbon PTL consists of a carbon fibre composite material with 5 wt% polytetrafluoroethylene (PTFE). The anode PTLs used are described in the following subsection. All PTLs were sealed by PTFE gaskets, with a thickness matching the thickness of the anode PTLs by \pm 5 μm and on average 100 μm less than the thickness of cathode PTL to achieve a compression of 29 % of the carbon PTL at dry state.

2.4. Anode porous transport layers

Within this work, two different types of titanium grade 1 PTLs were used: Commercially available titanium felts (TiF) with a thickness of $363 \pm 8 \,\mu m$, a porosity of $68 \,\%$ and a fibre diameter of $20 \,\mu m$ (NV Bekaert SA, Belgium), and titanium expanded metals (TiEM) from Bender GmbH Maschinenbau & Streckmetallfabrik (Germany) with a thickness of $136.5 \pm 3.5 \, \mu m$ (see Fig. 1a and b). The expanded metals exhibited an opening of 336 \pm 10 μ m x 190 \pm 15 μ m and open area of approximately 24.9 ±2.5%. Table 2 provides an overview of all the anode PTLs that were tested in PEMWE operation. After the PTLs were coated with Ti-Nb alloys on the MEA-facing side, the FF-facing side was coated with platinum to minimize oxidation and other forms of degradation on the back of the PTL and consequently to ensure that the performance and degradation of the novel alloy coating could be assessed independently from other corrosion effects. The platinum coating was deposited using a Quorum Q150T ES (Quorum Technologies Ltd). A thickness of $37.5 \pm 0.2\,\text{nm}$ was achieved, corresponding to a platinum loading of 0.06 mg_{Pt}cm⁻². The same Pt coating was deposited on both sides of the reference PTLs to investigate the cell performance with noble metal coated samples. To asses the performance with uncoated, pure Ti PTLs, Ti PTLs that were only coated with Pt on the FF-facing side were used.

Overview of the substrate and coating of all tested PTLs..

Sample	Substrate	Front coating
TiF_uncoated	Ti felt	uncoated
TiF_Pt	Ti felt	Pt
TiEM_uncoated	Ti expanded metal	uncoated
TiEM_Pt	Ti expanded metal	Pt
${\rm TiF_Ti}_{97}{\rm Nb}_3$	Ti felt	${\rm Ti}_{97}{\rm Nb}_3$
${\rm TiEM_Ti}_{97}{\rm Nb}_3$	Ti expanded metal	${\rm Ti}_{97}{\rm Nb}_3$
TiF_Ti ₉₄ Nb ₆ _1	Ti felt	$\mathrm{Ti}_{94}\mathrm{Nb}_{6}$
$TiF_Ti_{94}Nb_{6}_2$	Ti felt	$\mathrm{Ti}_{94}\mathrm{Nb}_{6}$
$TiEM_Ti_{94}Nb_6$	Ti expanded metal	$\mathrm{Ti}_{94}\mathrm{Nb}_{6}$
$\mathrm{TiF_Ti}_{72}\mathrm{Nb}_{28}$	Ti felt	$\mathrm{Ti}_{72}\mathrm{Nb}_{28}$
$\mathrm{TiEM_Ti}_{72}\mathrm{Nb}_{28}$	Ti expanded metal	${\rm Ti}_{72}{\rm Nb}_{28}$

The backsides of all PTLs were coated with Pt.

2.5. PEMWE test bench

An in-house built test bench providing five test places was used [19]. Each place was equipped with a peristaltic pump (Ismatec ISM832C) delivering water to the anode and cathode side at a rate of $25.0 \pm 1.5\,\mathrm{mL\,min^{-1}}$ on the anode and $24.0 \pm 2.5\,\mathrm{mL\,min^{-1}}$ on the cathode. The water supply on the cathode side prevents partial drying of the membrane near the cathode at high current densities, supports gas removal, and ensures uniform temperature conditioning of the cell. The water supplied to the cells was purified by a water treatment system (Merck Millipore) to a conductivity of $0.055\,\mu\mathrm{S\,cm^{-1}}$ and a total organic carbon content (TOC) of less than 3 ppb. As the excess water from the cell outlets returns to the tanks, ion exchangers (AmberliteTM IRN-150) were installed between the water storage tank and the cell inlet to ensure that no impurities enter the cells. Ni-Cr-Ni thermocuples were installed in each flow field plate and the temperature measured and controlled to 80 °C by an in-house built

heating box. A TDK Lambda GEN-20-76 DC power supply was used as current source (accuracy of voltage output: 10 mV; current output: 152 mA; readback current: 228 mA). Cell voltages were recorded using a Keithley model 2701 multimeter with an accuracy readback voltage of 10 mV. Further details about the test bench are given in [19].

2.6. PEMWE test protocol

Following the assembly of the cells, the cells and purified water were heated to the operating temperature of 80 °C. After 1h of heat up, the cell voltage was increased to 1.7 V in 0.05 V-steps per minute and held for a period of 15h for conditioning as proposed by Lickert et al. [20]. Subsequently, the first I-V curves were recorded to compare begin-of-test (BOT) performances. The I-V curves were recorded potentiostatically in 50 mV-steps from 1.3 V to 2.0 V, whereby the intervals between the voltage steps were chosen closer (between 20 mV to 30 mV) in the low voltage range to depict the initial curvature of the curve. Each voltage step was held for 5 min. The I-V curves were then generated from the mean values of the last 10 measuring points of a voltage step. Furthermore, electrochemical impedance (EIS) spectra were recorded. To record the spectra, the power supply from the test bench had to be interrupted and disconnected to connect the cell to a Biologic HCP 1005 potentiostat, including a booster unit to allow currents up to 100 A. Furthermore, the sense lines of the test bench were also removed to connect the potentiostat's sense lines. As only one cell could be connected to the potentiostat, all other cells that were not subject to the EIS measurement stayed at 1.45 V to protect the cells from a decreasing open circuit potential (OCP), as cycling between OCP and potentials above 1.40 V vs. RHE promotes iridium dissolution [21]. Spectra were recorded potentiostatically at 1.45 V, 1.50 V, 1.55 V, 1.60 V, 1.65 V, 1.70 V, 1.80 V, 1.90 V and 2.0 V in a frequency range between 100 mHz and 10 kHz and an amplitude of 5 mV. Impedance measurements were predominantly carried out to determine the high-frequency resistance (HFR), as the HFR represents the sum of all purely ohmic resistances composed of the resistance of the proton transport through the membrane and all transition resistances of metallic components. An increase of the HFR indicates, for example, increased contact resistance between the PTL and the CL, as the resistance of proton transport through the membrane is assumed to be constant under constant temperature conditions and without taking membrane creep into account. The HFR therefore provides a diagnostic tool for monitoring the PTL resistance. For the determination of HFR, the software ZView® from Scribner was used with the Calc-Modulus as type of data weighting where the error for the HFR always amounted for less than 1%. The equivalent circuit model used is displayed in the supplementary information (SI) in Figure S3. Afterwards, potentiostatic operation at 2.0 V was conducted for up to 672.5 h and interrupted for the recording of three consecutive I-V curves after 40 h, 144 h and at the end of test as well as for the recording of impedance spectra. Measurements with reference cells without Pt coating were conducted for 1005 h and with Pt coating for 457 h.

2.7. Interfacial contact resistance

A 4-wire setup was used to determine an approximation of the interfacial contact resistance (ICR) of the PTLs independently of all other cell components. For this purpose, the PTLs were placed between two compressible carbon PTLs (TGP-H-120 from Toray) under a gold-plated copper stamp. As the carbon PTLs are compressible, they served to compensate for inhomogeneities of the PTLs under investigation and thus to increase the contact area between the carbon PTLs and coated PTLs. The stamp was screwed to a pneumatic cylinder which is used to apply a constant force. For the measurements a pressure of 5.8 bar was applied, resulting in an average contact pressure of 1.53 MPa on the sample. To determine the through plane resistance, currents of 100 mA, 200 mA, 300 mA, 400 mA, 500 mA, 600 mA, 700 mA and 790 mA were

Table 3Overview of the coatings including the proportions of the elements determined by EDS and the layer thicknesses measured on the Si-wafers using ImageJ.

Coating	Ti/at.%	Nb /at.%	Thickness/μm
Ti ₉₇ Nb ₃	97.3 ± 0.04	2.6 ± 0.04	3.5 ± 0.01
${\rm Ti_{94}Nb_6}$	93.8 ± 0.04	6.1 ± 0.04	$4.1~\pm~0.01$
${\rm Ti}_{72}{\rm Nb}_{28}$	71.5 ± 0.1	28.5 ± 0.1	$4.4~\pm~0.1$

applied between both gold-plated copper plates by an SP-150 potentiostat from Biologic and the voltage drop at every current step was measured by the same potentiostat with two voltage sensing cables, one attached to the upper, one attached to the lower stamp. Figure S2 shows a schematic representation of the setup and the upper stamp that is attached to the pneumatic cylinder. The through plane resistances were then calculated from the slope of the I-V curves. The measurements and calculations were repeated three times and the slopes were averaged. To calculate the ICR, the system resistances were determined with the two carbon PTLs before and after each measurement and subtracted from the measured values with PTL. As the ICR between the two carbon PTLs cannot be determined, this unknown resistance comprises a systematic error in the determination of the PTL resistance. However, this error is expected to be similar for all measurements and is therefore assumed to not influence the determination of the change in ICRs of the PTLs. Furthermore, as the resistance of titanium in the bulk of the PTL is assumed to be negligible compared to the resistances of the PTL surface and coating, the calculated resistance can be approximated as interfacial contact resistance and assumed to be a property of the PTL surface.

3. Results

3.1. Coating deposition

Fig. 2(a) shows the three different coatings deposited as described in Section 2.1 on (100) oriented Si-wafers. Additionally, a magnified area of the $\rm Ti_{72}Nb_{28}$ coating acquired with a backscattered electron detector highlights the lamellar structure. This structure is representative of all coatings and becomes visible upon sufficient magnification. The ratio between titanium and niobium fractions of the coatings was determined using EDS point measurements. Minor amounts of oxygen detected by EDS were disregarded in the determination of the coating composition. The element percentages and coating thicknesses on the Si-wafers are summarized in Table 3. The coating thickness on the PTLs that were tested in the electrolyzer were in the same order of magnitude, but varied to a greater extent as the PTLs have more irregular surfaces, shown in the supplementary information Figure S4 and Figure S5.

Fig. 2(b) shows the SEM image and EDS analysis of a lamella that was cut out of a polished cross section of TiEM_Ti_{94}Nb_6. The individual lamellae are approximately $35\pm 5\,\mathrm{nm}$ thick. EDS point analysis show a range for the niobium content between 1 ± 0.4 at.% (red lamellae) to 10 ± 2 at.% (turquoise lamellae) and an overall niobium content of 6 ± 1 at.% measured over several lamellae using a line scan. Overall, this indicates that niobium is not homogeneously distributed within the coating, and that the amount of niobium present at the surface in contact with the MEA may differ. As can be seen in Figure S6 in the supplementary information, the lamellar structure of the coating remains intact after PEMWE operation.

3.2. PEMWE performance and impedance spectroscopy

To benchmark the novel coatings, PEMWE performance was first evaluated using titanium PTLs with and without Pt coatings towards the CL-facing side, with the latter serving as the performance target. I–V curves with uncoated and Pt coated titanium felt (TiF) and titanium

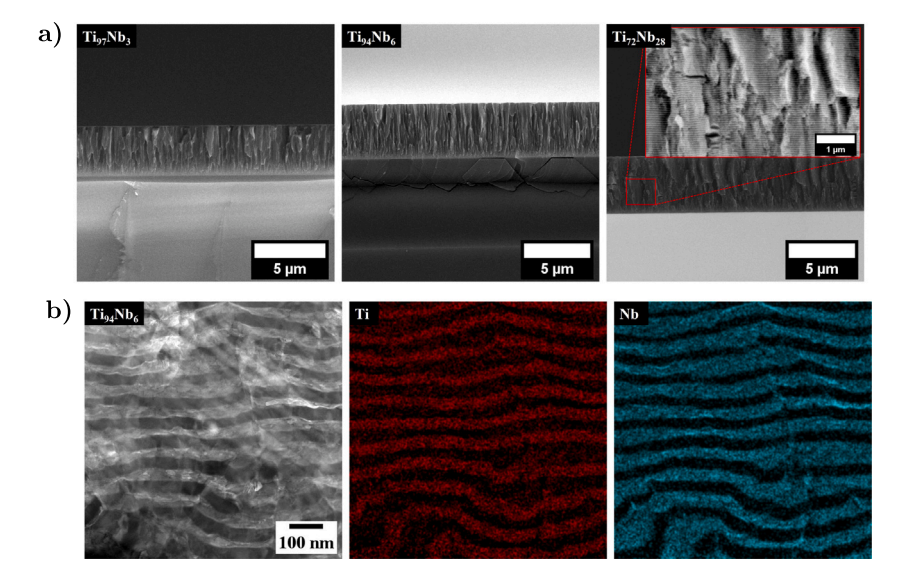


Fig. 2. (a) SEM images (secondary electron) of the different coatings with 3 at.%, 6 at.% and 28 at. % niobium, deposited on (100) oriented Si-wafers. The individual coatings were deposited in the same run in which the felts and expanded metals were coated. (b) SEM image and EDS analysis of a lamellar cut from $TiEM_{-}Ti_{94}Nb_{6}$. In the images, a distinct lamellar microstructure of the $Ti_{94}Nb_{6}$ coating is visible.

expanded metal (TiEM) are displayed in the supplementary information (Figure S7).

With Pt coated Ti felt (TiF_Pt, Figure S7a), the maximum current density at $2.0\,\mathrm{V}$ stayed at $2.9\,\mathrm{A}\,\mathrm{cm}^{-2}$ after an operation period of $457\,\mathrm{h}$ at $2.0\,\mathrm{V}$. Likewise, with TiEM_Pt, a stable performance of $2.3\,\mathrm{A}\,\mathrm{cm}^{-2}$ at $2.0\,\mathrm{V}$ was observed (Figure S7c). Without Pt coating, significantly lower current densities were reached as expected and a decrease in performance was observed, especially within the first $157\,\mathrm{h}$. During the experiment with uncoated TiF (Figure S7b), the water supply was interrupted unexpectedly, leading to superimposed MEA and PTL ageing. Nevertheless, a significantly reduced initial performance with uncoated TiF is evident in comparison to the performance with TiF_Pt.

The initial current density at 2.0 V with TiF_Ti₉₇Nb₃ was 1.1 A cm⁻² below the experiment with TiF_Pt (c.f. Fig. 3a and Figure S7a). A similar trend was observable with TiEM_Ti₉₇Nb₃, where the initial current density at 2.0 V after conditioning lay 0.55 A cm⁻² below the current density reached with TiEM_Pt (Figure S7c). As visible from the I–V curves displayed in Fig. 3, the performance with TiF and TiEM was unexpected close and in the same range within the expected measurement inaccuracy, most likely caused by manufacturing-related fluctuations. In contrast, the performance difference between the two Pt coated PTL substrates was considerably greater and amounted for 0.6 A cm⁻² (c.f. Figure S7a and c). After 144 h PEMWE operation at 2.0 V cell voltage, the maximum current densities dropped by 140 \pm 10 mA cm⁻² and HFRs increased between 20 m Ω cm² to 70 m Ω cm², whereby the HFR increase was less pronounced at small cell voltages (Fig. 3b and d).

Furthermore, while the ohmic resistance followed a clear trend, no clear trend was observed for kinetic overvoltages, as charge transfer resistances estimated from Nyquist plots decreased in the lower current density range, but trends in the higher current density range differed slightly between the two samples (Figure S12).

A more distinct difference in performance between the coated expanded metal and felt was observed with $Ti_{97}Nb_3$ coatings than with $Ti_{94}Nb_6$ coatings. The difference in current densities at 2.0 V between $TiF_Ti_{94}Nb_6_1$ and $TiEM_Ti_{94}Nb_6$ amounted for 0.44 A cm $^{-2}$ (Fig. 4). However, this only applied with $TiF_Ti_{94}Nb_6_1$. The performance with a second sample, TiF_Ti_{94} Nb_6_2 , was decreased (Fig. 4a) and below that of the similarly coated TiF. Furthermore, when comparing the HFR increase with $TiF_Ti_{94}Nb_6_2$ (60 m Ω cm 2 to 25 m Ω cm 2 , see Fig. 4c) with the HFR increase with Tig_Nb_3 coated PTLs ranging from 69 m Ω cm 2 to 22 m Ω cm 2 (Fig. 3c and d), it is noticeable that the performance development with $TiF_Ti_{94}Nb_6_2$ was closer to the observations with

 ${
m Ti}_{97}{
m Nb}_3$ coated samples than to the other two ${
m Ti}_{94}{
m Nb}_6$ coated samples. The same trend is reflected in the observed current density loss with these three samples (see Table 5). Nevertheless, with ${
m Ti}_{94}{
m Nb}_{6-1}$ and ${
m Ti}_{94}{
m Nb}_6$, an improved preservation of the PTL conductivity and thus stability could be observed compared to uncoated PTLs, as the current densities with these two PTLs decreased only by $30\,{\rm mA\,cm}^{-2}$, corresponding to an ageing rate of $0.2\,{\rm mA\,cm}^{-2}\,h^{-1}$, whereas the current density with uncoated TiEM decreased by $1.9\,{\rm mA\,cm}^{-2}\,h^{-1}$. For the calculation of the current density degradation with uncoated TiEM, the first $157\,h$ were considered (c.f. Figure S7d) to enable a comparison with the alloy coatings that were polarized for $144\,h$.

Increasing the niobium content to 28 at.% resulted in similar current densities at the beginning of the test as with other coatings investigated (c.f. Table 5), but after 144h a significantly greater increase in cell resistance and associated decrease in cell performance was observed (Fig. 5).

3.3. PTL resistances

ICRs of the PTLs were determined to identify trends and changes of the PTL conductivity. Although the ICR does not equal the contact resistance between PTL and CL during electrolysis operation, an increasing ICR due to oxidation or corrosion of the PTL surface adds to the overvoltages by increased ohmic losses.

Fig. 6 displays ICRs of all PTLs with alloy coatings. While the ICRs of pristine samples with $\rm Ti_{97}Nb_3$ and $\rm Ti_{94}Nb_6$ coatings ranged from $12\,m\Omega\,cm^2$ to $22\,m\Omega\,cm^2$, ICRs of PTLs with $\rm Ti_{72}Nb_{28}$ coatings accounted for around $41.5\,m\Omega\,cm^2$. ICRs of pristine PTLs with $\rm Ti_{97}Nb_3$ and $\rm Ti_{94}Nb_6$ coatings were close, as was expected due to their similar niobium content.

ICRs of pristine and aged uncoated TiEM as well as Pt coated TiEM are displayed in the supplementary information for comparison (Figure S8). The ICR of pristine uncoated TiEM was in a similar range than of TiEM coated with $Ti_{97}Nb_3$ and $Ti_{94}Nb_6$ and amounted for $11~\text{m}\Omega\,\text{cm}^2$. With uncoated TiEM, the ICR increased to $105~\text{m}\Omega\,\text{cm}^2$ after 1005 h at 2.0 V, while the ICR with Pt coating stayed at $3~\text{m}\Omega\,\text{cm}^2$ after 670 h. After 144 h of operation, resistances of samples with $Ti_{94}Nb_6$ coating increased by around $50~\text{m}\Omega\,\text{cm}^2$. The strongest increase was found with $Ti_{72}Nb_{28}$ coatings amounting for $92\pm2~\text{m}\Omega\,\text{cm}^2$ and $103\pm18~\text{m}\Omega\,\text{cm}^2$.

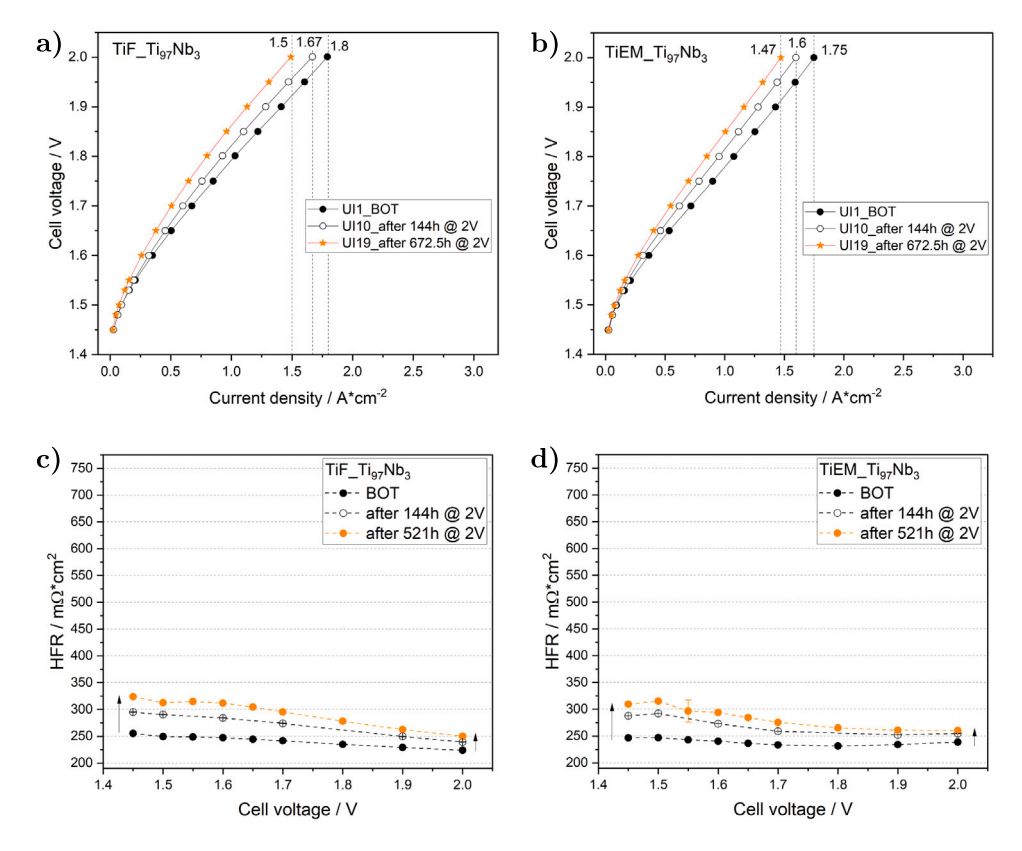


Fig. 3. I–V curves with Ti₉₇Nb₃ PVD coated PTLs: (a) titanium felt and (b) titanium expanded metal. Sub-figures (c) and (d) display corresponding HFRs extracted from EIS by means of equivalent circuit fitting. EIS was not performed after 672.5 h, but only after 521 h.

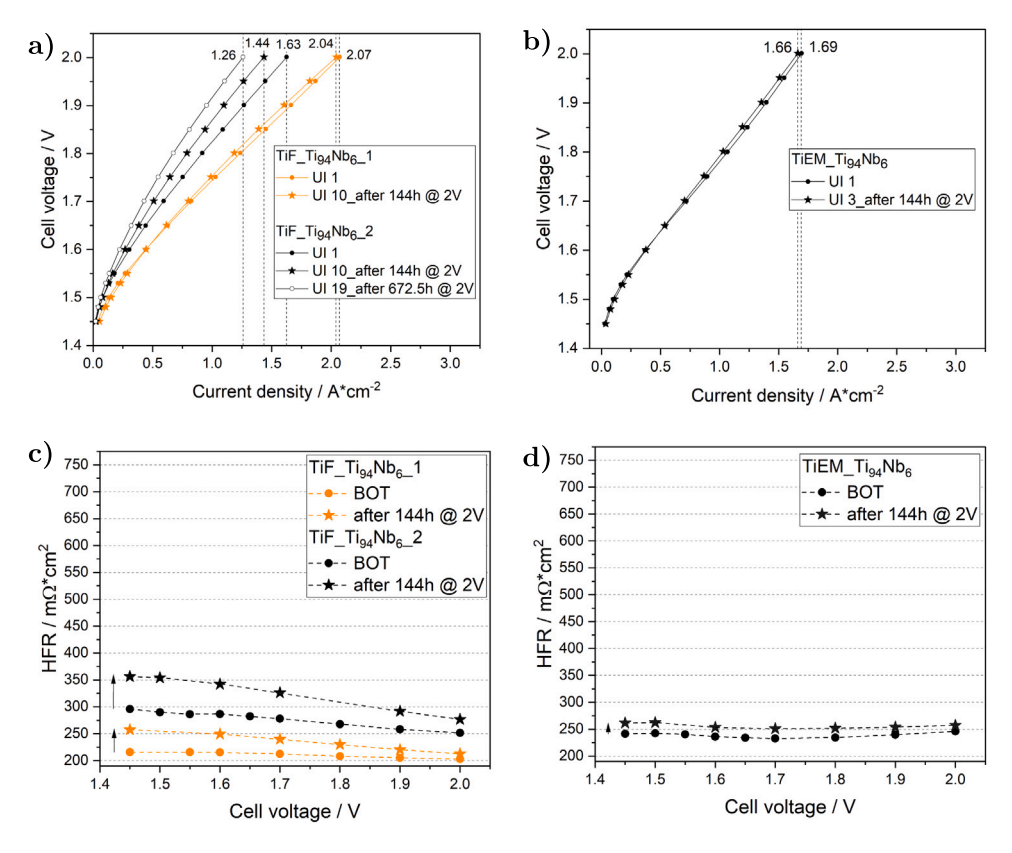


Fig. 4. I–V curves with Ti₉₄Nb₆ PVD coated PTLs: (a) two titanium felts and (b) titanium expanded metal. Sub-figures (c) and (d) display corresponding HFRs extracted from EIS by means of equivalent circuit fitting.

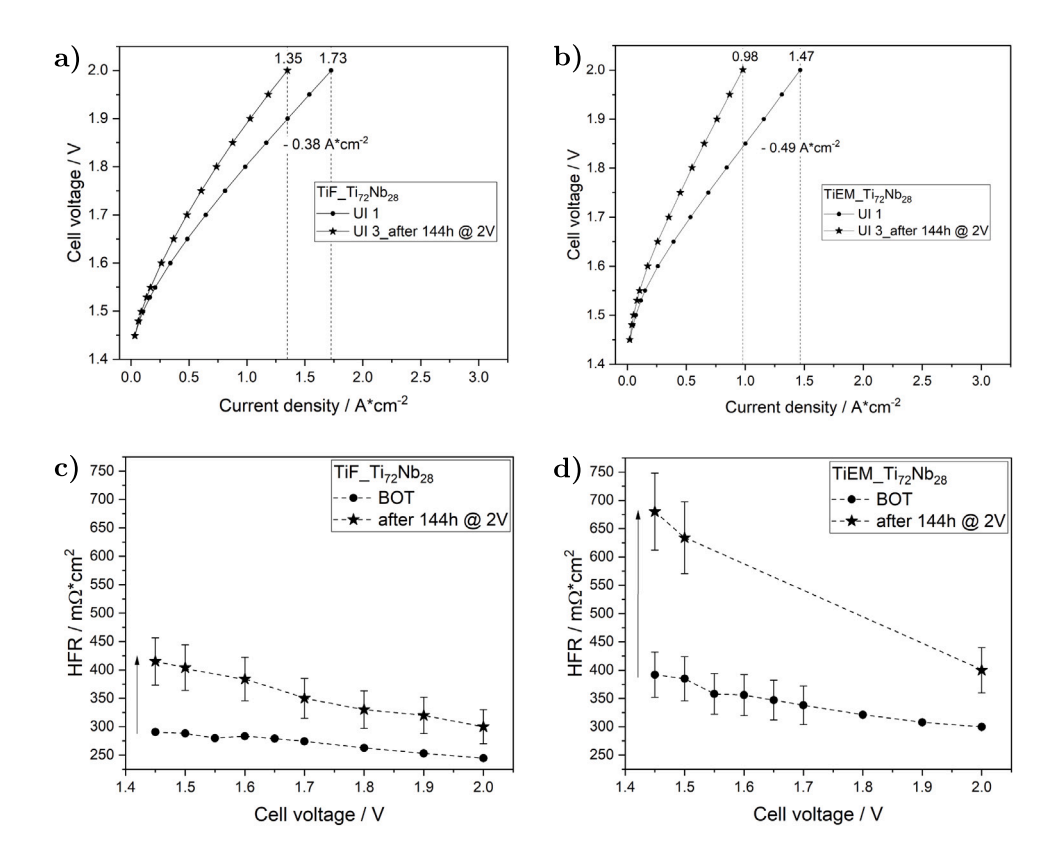


Fig. 5. I–V curves with $Ti_{72}Nb_{28}$ PVD coated PTLs: (a) titanium felt and (b) titanium expanded metal. Sub-figures (c) and (d) display corresponding HFRs extracted from EIS by means of equivalent circuit fitting. HFRs with larger error bars (10%) could not be determined using a fit as described in Section 2.6 due to capacities at high frequencies (see Figure S15). In these cases, the HFR was determined manually using a linear fit and extrapolation of the intersection with the real axis and is therefore subject to an augmented error.

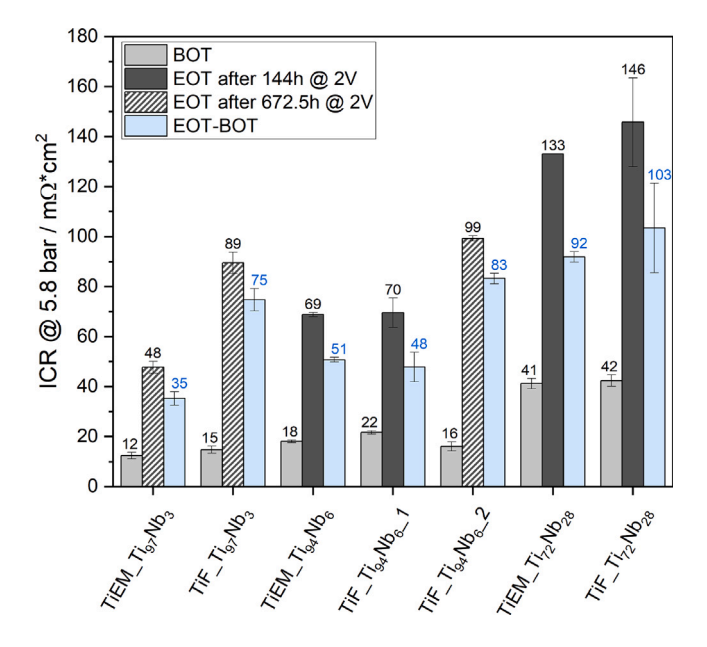


Fig. 6. ICRs of all investigated pristine and aged Ti-Nb-coated Ti PTLs with indication of the increase in resistance in blue. The measurements were carried out at 5.8 bar corresponding to a contact pressure of 1.53 MPa. The resistance of the Pt coated TiEM amounted for $3\,\mathrm{m}\Omega\,\mathrm{cm}^2$ (see Figure S8).

When PEMWE was conducted for 672.5 h, the ICR increase with $Ti_{97}Nb_3$ coatings and $Ti_{94}Nb_6$ coatings were more pronounced with $75\pm5\,\mathrm{m}\Omega\,\mathrm{cm}^2$ and $83\pm2\,\mathrm{m}\Omega\,\mathrm{cm}^2$, compared to shorter experiments.

As increasing ICRs were observed with all alloy coatings, none of the alloy coatings could provide the same conductivity as a noble metal coating.

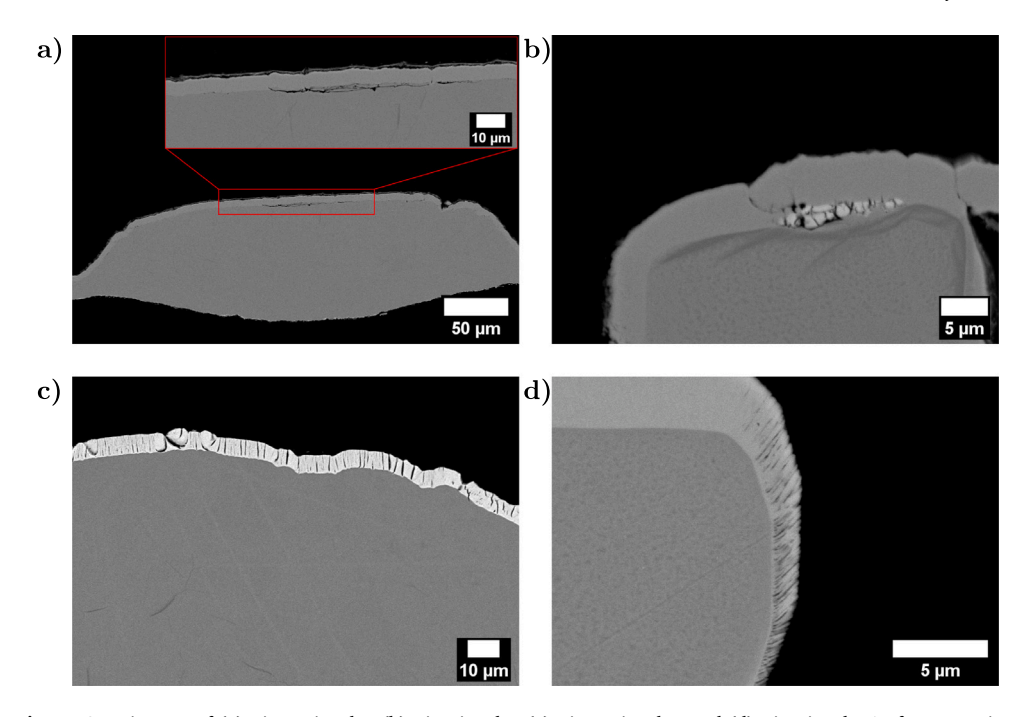
3.4. Post-mortem physico-chemical characterization

To investigate oxidation and degradation of the coatings and PTLs, they were examined by SEM, EDS and TEM after PEMWE operation.

SEM

EDS measurements were carried out on the surface of the MEAfacing side of the PTLs, compare Table 4. No clear correlation between the electrolysis operation and the determined oxygen content could be derived with the present standard deviation of the measurements.

Even though large parts of the PTLs, including the coatings, seemed to be unchanged after visual inspection, various spots of degradation, e.g. coating delamination or oxidation, were found on both the front and back of the PTLs. Furthermore, corrosion was found at some spots between the protective coating and the PTL, indicating that the coating was not sufficiently dense at all points to protect the underlying PTL. Fig. 7 shows the corrosion between the coating and the PTL on (a) TiEM_Ti97Nb3 and on (b) TiF_Ti97Nb3. Furthermore, (c) TiEM_Ti72Nb28 shows a large amount of vertical cracks in the coating, which were not observed in other coatings, including TiF_Ti72Nb28, which was coated simultaneously. On some of the coated fibres of the titanium felts a pronounced columnar structure can be observed on the edges perpendicular to the front, compare TiF_Ti94Nb6 (d) that can also affect the protective effect of the coating.



 $\textbf{Fig. 7.} \ \ \text{SEM images of (a)} \ \ \text{TiEM_Ti}_{97} \text{Nb}_3, \ \ \text{(b)} \ \ \text{TiF_Ti}_{97} \text{Nb}_3, \ \ \text{(c)} \ \ \text{TiEM_Ti}_{72} \text{Nb}_{28} \ \ \text{and (d)} \ \ \text{TiF_Ti}_{94} \text{Nb}_{6_1} \ \ \text{after operation}.$

Table 4EDS measurements of the MEA facing side of the PTLs after PEMWE operation.

Sample	Ti/at.%	Nb/at.%	O/at.%
TiEM_Ti ₉₇ Nb ₃	85 ± 2.3	2.5 ± 0.3	13 ± 2.3
$TiF_{27}Nb_{3}$	86 ± 4.5	2.3 ± 0.4	11 ± 4.5
${\rm TiEM_Ti}_{94}{\rm Nb}_6$	85 ± 5.9	5 ± 0.9	$11~\pm~5.1$
$\mathrm{TiF}_{-}\mathrm{Ti}_{94}\mathrm{Nb}_{6-}\mathrm{1}$	85 ± 6.7	5 ± 0.5	10 ± 7.2
$TiF_Ti_{94}Nb_{6}_2$	80 ± 1.4	5 ± 0.3	15 ± 1.4
${\rm TiEM_Ti}_{72}{\rm Nb}_{28}$	53 ± 10.3	18 ± 5.7	29 ± 9.4
$\mathrm{TiF_Ti}_{72}\mathrm{Nb}_{28}$	59 ± 5	25 ± 1	16 ± 5.8

TEM

In order to examine the oxide layer of TiEM_Ti₉₄Nb₆ more closely, a piece of the sample was electroplated with nickel, embedded and a cross-section was produced. Subsequently, a TEM lamella was cut out at the upper end of the coating, which was then analysed with EDS, see Fig. 8. The images and spectra revealed that a crack had formed between the nickel layer and the sample, most likely caused by the epoxy contracting during curing. This process pulled the oxide layer from the coating leaving it stuck on the nickel plating. As can be seen from the EDS mapping, this detached oxide layer contains homogeneously distributed titanium, oxygen and niobium. The results of the TEM analysis thus confirms that the introduction of Nb into titanium leads to the presence of niobium in the forming oxide layer.

4. Discussion

4.1. PTLs and coatings

The setup of the CC800/9 sputtering system, as described in Section 2.1, resulted in varying angles and distances between the targets and the rotating substrates, thereby influencing local growth rates and the composition of the coatings. This led to the formation of a lamellar structure composed of alternating layers with different niobium contents, as shown in Fig. 2. The inhomogeneous distribution of niobium, particularly near the surface, may affect the formation of the oxide

scale as well as the reproducibility of PEMWE experiments. However, the influence of the niobium distribution on oxide scale formation and experimental reproducibility was not examined within this study. Regarding the analysis of oxygen using EDS, it should be noted that the technique is not fully quantitative in this context, as oxygen is a light element and its signals partially overlap with those of titanium at low energies. In addition, the interaction volume includes both the oxide layer and parts of the underlying metallic coating, which may contain dissolved oxygen. The high standard deviation in the oxygen measurements makes interpretation difficult but also aligns with the observation that corrosion, or in this case oxidation of the PTLs, during operation may have occurred in a more localized and heterogeneous manner. The complex geometry of the PTLs, particularly their curvature, poses a significant challenge for uniform coating deposition. Although the coatings are largely dense, regions with cracks or pinholes remain, potentially compromising the protective effect, see Fig. 7. The inhomogeneous degradation of the PTLs was presumably caused by variations in contact pressure resulting from the land-and-channel structure of the flow field and defects in the coating structures such as pinholes or cracks, shown in Section 3.4. The degradation of the backside of the PTLs was not included in the presented results, as this study focuses on coatings on the CL-facing side and the measurements of performance and ICR on PTLs with Pt coating on both sides showed no degradation.

4.2. Electrolysis performance

The following Table 5 provides an overview of performance parameters from all PEMWE experiments. In addition, I–V curves and HFRs given in Section 3.2 and overviews of charge transfer resistances provided in the supplementary information in the figures S12 to S14 and serve as a base for the subsequent discussion of the results.

Comparative experiments with uncoated, pure Ti PTLs demonstrated that their initial performance is strongly influenced by their surface properties as well as storage times and the associated presumed differences in oxide scale thicknesses. Furthermore, the performance decrease with uncoated PTLs was caused by a growing titanium oxide layer at the PTL surface facing the CL [22], reflected by increasing HFRs (Figure S9b and S10b) and ICRs (Figure S8). Further comparative

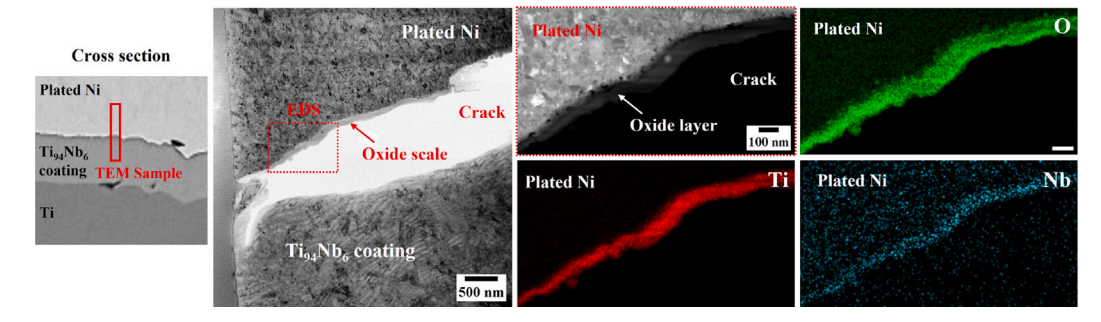


Fig. 8. TEM analysis of TiEM_Ti₉₄Nb₆ after 144h of PEMWE operation. Part of the PTL was nickel plated before a lamella was cut out of a cross section and EDS was conducted showing the presence of O, Ti and Nb in the oxide layer.

Table 5Overview of performance parameters from PEMWE experiments.

Sample	Current density at 2.0 V BOT/A * cm ⁻²	Current density drop at 2.0 V after $144 h/mA * cm^{-2}$	HFR increase ^{1,2} $/m\Omega * cm^2$
TiEM_Ti ₉₄ Nb ₆	1.69	30	20-11
$\mathrm{TiF_Ti}_{94}\mathrm{Nb}_{6_}1$	2.07	30	42-10
$\rm TiF_Ti_{94}Nb_{6}_2$	1.63	190	60-2
$TiEM_Ti_{97}Nb_3$	1.75	150	68-22
TiF_Ti ₉₇ Nb ₃	1.80	130	69-27
$\mathrm{TiEM_Ti}_{72}\mathrm{Nb}_{28}$	1.47	490	288-100
$\mathrm{TiF_Ti}_{72}\mathrm{Nb}_{28}$	1.73	380	124-45
TiF_uncoated	0.826	not applicable	not applicable
TiF_Pt	2.91	<0.04	/
TiEM_uncoated	1.37	290 ³	not applicable
TiEM_Pt	2.31	< 0.05	/

1: after 144 h, 2: ranges due to distribution between low and high cell voltages, 3: after 157 h.

experiments with state-of-the-art Pt-coated PTLs showed that the Pt coating not only influenced the contact resistance between PTL and CL and thus the ohmic resistance, but also the kinetics of water splitting, as impedance spectra revealed increasing low-frequency resistances for uncoated PTLs (see Figure S9b and Figure S10b). A degradation process of IrO2 in combination with uncoated Ti PTLs leading to increased CT resistances was suggested by Liu et al. [22] involving oxygen that is transferred from IrO2 to titanium forming unstable iridium species, whereby this hypothesis is not experimentally validated, but also conceivable for alloy coatings. In addition, a feature at high frequencies appeared in the Nyquist plots with uncoated PTLs. An increasing imaginary impedance at high frequencies was also reported by Siracusano et al. [23] and attributed to capacitive behaviour caused by a high contact resistance and junction effect between the electrode and bipolar plate. This capacitive effect at high frequencies caused by charge accumulation at the TiO_x-layer impedes the imaginary impedance to become zero and consequently the Z'-axis is not reached in the Nyquist plot, unlike with Pt-coated PTLs, where an ohmic contact between the PTL and the CL is present. The same capacitive effect was observed with TiEM_Ti₇₂Nb₂₈ after 144h (Figure S15). Hence, a similar oxidation behaviour and thus a similar ageing pathway can be assumed for this alloy coating as for pure Ti coatings.

Furthermore, with uncoated and Ti₇₂Nb₂₈-coated PTLs, a shifting HFR towards lower resistances at higher cell voltages was observed, presumably caused by the production of heat [24]. As the thermal conductivities of titanium and niobium oxides are lower compared to the pure metals and Pt [25–29], local hotspots can form when the coatings oxidize. Although thermal conductivities are not available for Ti-Nb mixed oxides, it is likely that the thermal conductivities of the mixed oxides are also decreased compared to the pure metallic alloy. Even though hotspots can increase the proton conductivity of the membrane and thus reduce the cell resistance [30], local temperature

increases pose the risk of membrane thinning [31], leading to MEA failure during prolonged operation.

Regarding the surface oxygen content of the alloy coatings, a trend became apparent, suggesting a correlation between an increasing surface oxygen content and decreasing current density during electrolysis. With the sample ${\rm TiEM_Ti_{72}Nb_{28}}$, which exhibited the highest oxygen content post-mortem, also the most pronounced performance loss was observed after 144 h, followed by ${\rm TiF_Ti_{72}Nb_{28}}$, which ranked second in both post-mortem oxygen content and current density decline (see Fig. 5 and Table 5). The higher niobium content of 28 at.% might have led to an even more pronounced heterogeneous distribution of niobium within the coating compared to coatings with lower niobium content and an oxide phase separation in the scale.

In contrast, TiEM_Ti $_{94}$ Nb $_{6}$ and TiF_Ti $_{94}$ Nb $_{6}$ 1 contained the lowest post-mortem oxygen concentrations of 10 at.% and 11 at.% (Table 4) and enabled the maintenance of stable current densities (see Fig. 4). However, these promising results with TiF_Ti $_{94}$ Nb $_{6}$ 1 could not be reproduced with a second sample (TiF_Ti $_{94}$ Nb $_{6}$ 2), that was operated for 672.5 h instead of 144 h where a notable drop in current density and increased ICR was measured. EDS analysis revealed, that TiF_Ti $_{94}$ Nb $_{6}$ 2 exhibited a post-mortem oxygen content that was approximately 5 at.% higher than at the surface of TiF_Ti $_{94}$ Nb $_{6}$ 1. Furthermore, increasing charge transfer resistances were also observed with TiF_Ti $_{94}$ Nb $_{6}$ 2 (Figure S13b) like with uncoated PTLs (c.f. Figure S9b and S10b), leading to the conclusion that the underlying ageing pathways are similar.

It can therefore be concluded that the performance differences between the formally identical coatings with 6 at.% Nb are attributable to the properties of the coatings and not to other effects of the experiments, such as different test cells, MEAs, or temporal factors. Results from experiments demonstrating the reproducibility of PEMWE single-cell tests with Pt-coated standard PTLs are included in the supplementary information Figure S11.

 $TiF_Ti_{97}Nb_3$ and $TiEM_Ti_{97}Nb_3$ exhibited slightly lower postmortem oxygen contents than expected based on the fact that they were also operated for 672.5 h, where a drop in current density was observed, similar to $TiF_Ti_{94}Nb_{6_}2$.

As increasing ICRs were observed with all alloy coatings, none of the alloy coatings could provide the same conductivity as a noble metal coating. However, with regard to the ICR measurements, a discrepancy was observed: despite the ICR of two of the Ti₉₄Nb₆-coated samples increased, only a negligible loss in current density of $30\,\mathrm{mA\,cm^{-2}}$ was recorded. Consequently, no direct correlation between the ex-situ measured ICR and the electrochemical performance could be established. This discrepancy between the ex-situ measured ICRs and the actual contact resistances between the PTL and CL in the PEMWE cell may be attributed to locally higher contact pressures in the PEMWE cell caused by the channel-land structure of the meander flow field. At the edges of the land areas, the contact pressure can reach values between 3 MPa to 3.5 MPa [32], exceeding 1.5 MPa that were applied in the ICR setup. These locally elevated pressures can lead to lower contact resistances in the cell, partially compensating for the differences observed in the ex-situ measured ICRs.

In summary, the observed decrease in current density during electrolysis with $\rm Ti_{97}Nb_3$, $\rm Ti_{72}Nb_{28}$ and one $\rm Ti_{94}Nb_6$ coating is most plausibly attributed to a combination of oxidation processes decreasing the conductivity of the Ti-Nb-based protective layers and localized corrosion phenomena, which are likely facilitated by defects in the deposited coatings and may be further exacerbated by the unevenly distributed contact pressure. Furthermore, we assume that the additional presence of niobium in the oxide layer, detected through TEM (Fig. 8) provides additional donor sites which improve the conductivity of the oxide layer [15,17,18] and presumably is the reason that $\rm TiEM_Ti_{94}Nb_6$ and $\rm TiF_Ti_{94}Nb_6$.1 showed almost no decrease in current density during 144 h of PEMWE. The results with the $\rm Ti_{94}Nb_6$ coatings indicate the potential of Ti-Nb alloy coatings for anode PTLs. However, further improvements have to be made with regards to the coating homogeneity, alloy composition and oxide scale adhesion.

5. Conclusion

Three new titanium-niobium-alloys with 3 at.%, 6 at.% and 28 at.% niobium were investigated as potential protective layers for anode PTLs for PEM water electrolyzers. PTLs coated with alloys containing 6 at.% Nb (Ti₉₄Nb₆) reached promising current densities of 2.1 A cm⁻² at 2.0 V and the stability of PEMWE operation was enhanced compared to uncoated PTLs and close to the stability achieved with Pt coated PTLs. Almost stable PEMWE operation for 144h with titanium expanded mesh and felt PTLs with $\mathrm{Ti}_{94}\mathrm{Nb}_6$ coatings was reflected by a minor drop in current density at 2.0 V of only 30 mA cm⁻² and supported by impedance measurements. After electrolysis operation, it was possible to detect the presence of niobium in the oxide layer. We assume that the presence of Nb in the titanium oxide layer lead to donor sites in the scale for conduction as niobium has a higher valence than titanium. Furthermore, it is possible that the presence of niobium in the coating inhibited oxide growth on the coating as described in the literature [14]. Unfortunately, it was not yet possible to reproduce the results with Ti₉₄Nb₆ coatings. This might stem from the heterogeneous distribution of niobium or could result from the complex geometries of the PTLs, complicating the formation of a fully dense and well-adhering coating and might be also related to the low adherence of the formed oxide scale. Although the performance with alloy coatings was not yet competitive to noble metal coatings, their stability outperformed all other noble metal free coatings so far and showed a very promising approach to coat PTLs without precious metals in the future.

6. Outlook

Our results open up further avenues of research into other alloys with elements of different valence. Additionally, the coating process should be further investigated regarding the coating density and the impact of the distribution of elements. These improvements could be achieved by sputtering with a pre-alloyed target, thermal annealing after sputtering or a sputtering system in which the targets are on the same side of the sample and keep a rather constant distance. This would enable a systematic investigation of the effect of the lamellar structure on the coating performance. Once the most suitable alloy has been identified, the next step could be to produce powders with the same composition to use for coating deposition via cold gas spraying, as cold gas spraying has already been proven to be suitable for deposition on expanded metals and would enable a highly scalable vacuum-free coating method [33].

CRediT authorship contribution statement

Tim Sievert: Writing - review & editing, Writing - original draft, Visualization, Validation, Methodology, Investigation, Formal analysis, Data curation, Conceptualization. Sarah Zerressen: Writing - review & editing, Writing - original draft, Visualization, Validation, Methodology, Investigation, Formal analysis, Data curation, Conceptualization. Andreas Glüsen: Writing - review & editing, Supervision, Resources, Project administration, Funding acquisition, Conceptualization. Martin Bram: Writing - review & editing, Supervision. Sven Uhlenbruck: Writing - review & editing, Resources. Klaus Bender: Resources. Frank Vondahlen: Investigation. Ping Xiao: Writing - review & editing, Resources. Xuezhen Cao: Writing - review & editing, Investigation. Olivier Guillon: Writing - review & editing, Resources. Ralf Peters: Writing - review & editing, Supervision. Martin Müller: Funding acquisition, Conceptualization. Ulf-Peter Apfel: Writing - review & editing, Supervision. Robert Vaßen: Writing - review & editing, Supervision, Resources, Project administration, Funding acquisition, Conceptualization.

Declaration of competing interest

The authors declare that they have no known competing financial interests or personal relationships that could have appeared to influence the work reported in this paper.

Acknowledgements

This work was funded by the Federal Ministry of Research, Technology and Space (BMFTR), Förderkennzeichen 03ZU1115JC. Funding is highly acknowledged.

Furthermore, we gratefully acknowledge the preparation of membrane electrode assemblies by Daniel Holtz (IET-4).

Appendix A. Supplementary data

Supplementary material related to this article can be found online at https://doi.org/10.1016/j.jpowsour.2025.238944.

Data availability

Data will be made available on request.

References

- [1] L. Chaabane, L. Dammak, V.V. Nikonenko, G. Bulvestre, B. Auclair, The influence of absorbed methanol on the conductivity and on the microstructure of ionexchange membranes, J. Membr. Sci. 298 (1–2) (2007) 126–135, http://dx.doi. org/10.1016/j.memsci.2007.04.010.
- [2] L. Stein, A. Dittrich, D.C. Walter, P. Trinke, B. Bensmann, R. Hanke-Rauschenbach, Degradation of PGM and PGM-free coatings on PEMWE porous transport layers, ACS Appl. Mater. Interfaces (2025) http://dx.doi.org/10.1021/acsami.4c22455.
- [3] C. Wang, K. Lee, C.P. Liu, D. Kulkarni, P. Atanassov, X. Peng, I.V. Zenyuk, Design of PEM water electrolysers with low iridium loading, Int. Mater. Rev. 69 (1) (2024) 3–18, http://dx.doi.org/10.1177/09506608231216665.
- [4] K. Ayers, N. Danilovic, R. Ouimet, M. Carmo, B. Pivovar, M. Bornstein, Perspectives on low-temperature electrolysis and potential for renewable hydrogen at scale, Annu. Rev. Chem. Biomol. Eng. 10 (1) (2019) 219–239, http://dx.doi.org/10.1146/annurev-chembioeng-060718-030241.
- [5] M. Prestat, Corrosion of structural components of proton exchange membrane water electrolyzer anodes: A review, J. Power Sources 556 (2023) 232469, http://dx.doi.org/10.1016/j.jpowsour.2022.232469.
- [6] S. Stiber, N. Sata, T. Morawietz, S.A. Ansar, T. Jahnke, J.K. Lee, A. Bazylak, A. Fallisch, A.S. Gago, K.A. Friedrich, A high-performance, durable and low-cost proton exchange membrane electrolyser with stainless steel components, Energy Environ. Sci. (2022) http://dx.doi.org/10.1039/D1EE02112E.
- [7] A. Kellenberger, N. Vaszilcsin, D. Duca, M.L. Dan, N. Duteanu, S. Stiber, T. Morawietz, I. Biswas, S.A. Ansar, P. Gazdzicki, F.J. Wirkert, J. Roth, U. Rost, M. Brodmann, A.S. Gago, K.A. Friedrich, Towards replacing titanium with copper in the bipolar plates for proton exchange membrane water electrolysis, Materials 15 (5) (2022) 1628, http://dx.doi.org/10.3390/ma15051628.
- [8] O. Sorsa, J. Nieminen, P. Kauranen, T. Kallio, Stable reference electrode in polymer electrolyte membrane electrolyser for three-electrode measurements, J. Electrochem. Soc. 166 (16) (2019) F1326–F1336, http://dx.doi.org/10.1149/2. 0461916jes.
- [9] A. Hartig-Weiß, M. Bernt, A. Siebel, H.A. Gasteiger, A platinum micro-reference electrode for impedance measurements in a PEM water electrolysis cell, J. Electrochem. Soc. 168 (11) (2021) 114511, http://dx.doi.org/10.1149/1945-7111/ac3717.
- [10] E. Brightman, J. Dodwell, N. van Dijk, G. Hinds, In situ characterisation of PEM water electrolysers using a novel reference electrode, Electrochem. Commun. 52 (2015) 1–4, http://dx.doi.org/10.1016/j.elecom.2015.01.005.
- [11] H. Becker, E.J.F. Dickinson, X. Lu, U. Bexell, S. Proch, C. Moffatt, M. Stenström, G. Smith, G. Hinds, Assessing potential profiles in water electrolysers to minimise titanium use, Energy Environ. Sci. 15 (6) (2022) 2508–2518, http://dx.doi.org/ 10.1039/D2EE00876A.
- [12] A. Kellenberger, Electrochemical evaluation of niobium corrosion resistance in simulated anodic PEM electrolyzer environment, Int. J. Electrochem. Sci. (2020) 10664–10673, http://dx.doi.org/10.20964/2020.11.47.
- [13] S. Ramos, B. Canut, R. Brenier, L. Gea, L. Romana, M. Brunel, P. Thevenard, Electrical conductivity in niobium implanted TiO₂ rutile, Nucl. Instrum. Methods Phys. Res. Sect. B: Beam Interactions Mater. Atoms 80–81 (1993) 1123–1127, http://dx.doi.org/10.1016/0168-583X(93)90750-Z.
- [14] P. Pérez, V.A.C. Haanappel, M.F. Stroosnijder, The effect of niobium on the oxidation behavior of titanium in Ar/20% O₂ atmospheres, Oxid. Met. 53 (5/6) (2000) 481–506, http://dx.doi.org/10.1023/A:1004680909484.
- [15] N. Aukland, A. Boudina, D.S. Eddy, J.V. Mantese, M.P. Thompson, S.S. Wang, Alloys that form conductive and passivating oxides for proton exchange membrane fuel cell bipolar plates, J. Mater. Res. 19 (6) (2004) 1723–1729, http: //dx.doi.org/10.1557/JMR.2004.0216.
- [16] R.J. Hanrahan, D.P. Butt, Oxidation kinetics and mechanisms of Ti-Ta alloys, Oxid. Met. 47 (3-4) (1997) 317-353, http://dx.doi.org/10.1007/BF01668517.
- [17] G.D. Gesesse, O. Debieu, A. Jolivet, C. Frilay, S. Duprey, P. Marie, X. Portier, F. Lemarié, C. Labbé, C. Dufour, C. Grygiel, C. Labrugère, M. El-Roz, J. Cardin, Enhanced optical and electrical properties of Nb-doped TiO2 thin films synthesized by atomic layer deposition using the supercycle strategy, J. Alloy. Compd. Commun. 3 (2024) 100018, http://dx.doi.org/10.1016/j.jacomc.2024.100018.

- [18] M. Frisch, J. Laun, J. Marquardt, A. Arinchtein, K. Bauerfeind, D. Bernsmeier, M. Bernicke, T. Bredow, R. Kraehnert, Bridging experiment and theory: enhancing the electrical conductivities of soft-templated niobium-doped mesoporous titania films, Phys. Chem. Chem. Phys.: PCCP 23 (5) (2021) 3219–3224, http://dx.doi.org/10.1039/D0CP06544G.
- [19] S.-V. Pape, S. Zerressen, M.F. Seidler, R. Keller, F. Lohmann-Richters, M. Müller, U.-P. Apfel, A.K. Mechler, A. Glüsen, Performance data extraction from dynamic long-term operation of proton exchange membrane and alkaline water electrolysis cells, Int. J. Hydrog. Energy 127 (2025) 51–63, http://dx.doi.org/10.1016/j.ijhydene.2025.03.387.
- [20] T. Lickert, S. Fischer, J.L. Young, S. Klose, I. Franzetti, D. Hahn, Z. Kang, M. Shviro, F. Scheepers, M. Carmo, T. Smolinka, G. Bender, S. Metz, Advances in benchmarking and round robin testing for PEM water electrolysis: Reference protocol and hardware, Appl. Energy 352 (2023) 121898, http://dx.doi.org/10.1016/j.apenergy.2023.121898.
- [21] M. Bernt, A. Hartig-Weiß, M.F. Tovini, H.A. El-Sayed, C. Schramm, J. Schröter, C. Gebauer, H.A. Gasteiger, Current challenges in catalyst development for PEM water electrolyzers, Chem. Ing. Tech. 92 (1–2) (2020) 31–39, http://dx.doi.org/ 10.1002/cite.201900101.
- [22] C. Liu, M. Shviro, A.S. Gago, S.F. Zaccarine, G. Bender, P. Gazdzicki, T. Morawietz, I. Biswas, M. Rasinski, A. Everwand, R. Schierholz, J. Pfeilsticker, M. Müller, P.P. Lopes, R.-A. Eichel, B. Pivovar, S. Pylypenko, K.A. Friedrich, W. Lehnert, M. Carmo, Exploring the interface of skin-layered titanium fibers for electrochemical water splitting, Adv. Energy Mater. 11 (8) (2021) 2002926, http://dx.doi.org/10.1002/aenm.202002926.
- [23] S. Siracusano, V. Baglio, A. Di Blasi, N. Briguglio, A. Stassi, R. Ornelas, E. Trifoni, V. Antonucci, A.S. Aricò, Electrochemical characterization of single cell and short stack PEM electrolyzers based on a nanosized IrO₂ anode electrocatalyst, Int. J. Hydrog. Energy 35 (11) (2010) 5558–5568, http://dx.doi.org/10.1016/j.iihydene.2010.03.102.
- [24] M. Bühler, F. Hegge, P. Holzapfel, M. Bierling, M. Suermann, S. Vierrath, S. Thiele, Optimization of anodic porous transport electrodes for proton exchange membrane water electrolyzers, J. Mater. Chem. A 7 (47) (2019) 26984–26995, http://dx.doi.org/10.1039/C9TA08396K.
- [25] T. Schuler, R. de Bruycker, T.J. Schmidt, F.N. Büchi, Polymer electrolyte water electrolysis: Correlating porous transport layer structural properties and performance: Part I. Tomographic analysis of morphology and topology, J. Electrochem. Soc. 166 (4) (2019) F270–F281, http://dx.doi.org/10.1149/2. 0561904jes.
- [26] Z. Kang, T. Schuler, Y. Chen, M. Wang, F.-Y. Zhang, G. Bender, Effects of interfacial contact under different operating conditions in proton exchange membrane water electrolysis, Electrochim. Acta 429 (2022) 140942, http://dx. doi.org/10.1016/j.electacta.2022.140942.
- [27] C.J. Smithells, E.A. Brandes, Smithells Metals Reference Book, Seventh ed., Butterworths/Heinemann, 1992.
- [28] D. Music, S. Prünte, P. Keuter, A. Saksena, On thermal conductivity of amorphous niobium monoxide, J. Phys. D: Appl. Phys. 53 (28) (2020) 285303, http://dx. doi.org/10.1088/1361-6463/ab8517.
- [29] H.J. Cho, G. Kim, T. Onozato, H. Jeen, H. Ohta, Thermal conductivity tensor of NbO₂, Int. J. Heat Mass Transfer 137 (2019) 263–267, http://dx.doi.org/10. 1016/j.ijheatmasstransfer.2019.03.135.
- [30] J. Parra-Restrepo, Caractérisation des hétérogénéités de fonctionnement et de dégradation au sein d'un électrolyseur à membrane échangeuse de protons (PEM) (Ph.D. thesis), Université de Lorraine, 2020.
- [31] P. Millet, A. Ranjbari, F. de Guglielmo, S.A. Grigoriev, F. Auprêtre, Cell failure mechanisms in PEM water electrolyzers, Int. J. Hydrog. Energy 37 (22) (2012) 17478–17487, http://dx.doi.org/10.1016/j.ijhydene.2012.06.017.
- [32] S. Holtwerth, Mechanisches Verhalten von Polymer-Elektrolyt-Membran-Elektrolysezellen und -Stacks (Ph.D. thesis), RWTH Aachen, Aachen, 2022
- [33] T. Sievert, S. Zerressen, M. Bram, A. Glüsen, K. Bender, O. Guillon, R. Vaßen, Cold gas spraying of titanium on stainless steel to enhance corrosion protection inside proton exchange membrane water electrolyzers, Surf. Coat. Technol. (2025) 132486, http://dx.doi.org/10.1016/j.surfcoat.2025.132486, Publisher: Elsevier BV.